WATER VAPOR IN NEARBY INFRARED GALAXIES AS PROBED BY *HERSCHEL**

CHENTAO YANG (杨辰涛)[1,2,3], YU GAO (高煜)[2], A. OMONT[4,5], DAIZHONG LIU (刘岱钟)[2,3], K. G. ISAAK[6],
D. DOWNES[7], P. P. VAN DER WERF[8], AND NANYAO LU[9]

[1] Department of Astronomy, Beijing Normal University, Beijing 100875, China
[2] Purple Mountain Observatory/Key Lab of Radio Astronomy, Chinese Academy of Sciences, Nanjing 210008, China
[3] University of Chinese Academy of Sciences, Beijing, China
[4] Institut d'Astrophysique de Paris, UPMC Université Paris 06, UMR7095, F-75014 Paris, France
[5] CNRS, UMR7095, Institut d'Astrophysique de Paris, F-75014 Paris, France
[6] ESA Astrophysics Missions Division, ESTEC, P.O. Box 299, 2200 AG Noordwijk, The Netherlands
[7] Institut de Radioastronomie Millimétrique (IRAM), 300 rue de la Piscine, F-38406 Saint-Martin d'Hères, France
[8] Leiden Observatory, Leiden University, Post Office Box 9513, NL-2300 RA Leiden, The Netherlands
[9] Infrared Processing and Analysis Center, California Institute of Technology, MS 100-22, Pasadena, CA 91125, USA

ABSTRACT

We report the first systematic study of the submillimeter water vapor rotational emission lines in infrared (IR) galaxies based on the Fourier Transform Spectrometer (FTS) data of *Herschel* SPIRE. Among the 176 galaxies with publicly available FTS data, 45 have at least one H_2O emission line detected. The H_2O line luminosities range from $\sim 1 \times 10^5\ L_\odot$ to $\sim 5 \times 10^7\ L_\odot$ while the total IR luminosities (L_{IR}) have a similar spread (~ 1–$300 \times 10^{10}\ L_\odot$). In addition, emission lines of H_2O^+ and $H_2^{18}O$ are also detected. H_2O is found, for most galaxies, to be the strongest molecular emitter after CO in FTS spectra. The luminosity of the five most important H_2O lines is near-linearly correlated with L_{IR}, regardless of whether or not strong active galactic nucleus signature is present. However, the luminosity of $H_2O(2_{11}$–$2_{02})$ and $H_2O(2_{20}$–$2_{11})$ appears to increase slightly faster than linear with L_{IR}. Although the slope turns out to be slightly steeper when $z \sim 2$–4 ULIRGs are included, the correlation is still closely linear. We find that L_{H_2O}/L_{IR} decreases with increasing f_{25}/f_{60}, but see no dependence on f_{60}/f_{100}, possibly indicating that very warm dust contributes little to the excitation of the submillimeter H_2O lines. The average spectral line energy distribution (SLED) of the entire sample is consistent with individual SLEDs and the IR pumping plus collisional excitation model, showing that the strongest lines are $H_2O(2_{02}$–$1_{11})$ and $H_2O(3_{21}$–$3_{12})$.

Key words: galaxies: ISM – galaxies: starburst – infrared: ISM – ISM: molecules

Online-only material: color figures

1. INTRODUCTION

H_2O can be one of the most abundant oxygen molecular carriers besides CO in the warm interstellar gas (but it is mostly locked in icy interstellar dust grains in cold regions of the Galaxy; e.g., Melnick & Bergin 2005; van Dishoeck et al. 2011). Nevertheless, the study of the rotational H_2O line is always far more challenging than CO at low redshift. The main difficulty is from the contamination of the H_2O in the Earth's atmosphere. However, some pioneering research with the *Infrared Space Observatory* (covering ~ 2–$200\ \mu$m; Kessler et al. 1996) of both star-forming regions within our Galaxy, such as Orion (Harwit et al. 1998), and nearby galaxies, such as Arp220 (González-Alfonso et al. 2004), NGC 253 and NGC 1068 (Goicoechea et al. 2005), and Mrk231 (González-Alfonso et al. 2008), revealed that H_2O lines likely trace the local infrared radiation field (IRF) directly, and thus provide a unique diagnostic probing the physical and chemical processes, unlike other gas tracers such as CO. The *Herschel Space Observatory* (Pilbratt et al. 2010), with great improvement of sensitivity, angular resolution, and band coverage, offers an unprecedented opportunity to study the submillimeter regime of galaxies without atmospheric contamination, and thus provides unique chances to observe the H_2O lines within the SPIRE band (194–672 μm; Griffin et al. 2010).

Herschel has revealed a wealth of submillimeter H_2O lines in, e.g., Mrk231 (van der Werf et al. 2010; González-Alfonso et al. 2010, G-A10 hereafter), Arp220 (Rangwala et al. 2011;

González-Alfonso et al. 2012, 2013), NGC 4418 (González-Alfonso et al. 2012), NGC 1068 (Spinoglio et al. 2012), NGC 6240 (Meijerink et al. 2013), and M82 (Kamenetzky et al. 2012), from the energy level $E_{up}/k = 53$ K up to $E_{up}/k = 642$ K. Moreover, some detections from the ground in high-z ultra-luminous IR galaxies (ULIRGs) were also reported (e.g., Omont et al. 2011, 2013; van der Werf et al. 2011; Combes et al. 2012; Riechers et al. 2013). H_2O line strength is found to be comparable with neighboring high-J CO lines ($J = 8$–7 to $J = 13$–12) in these studies.

By modeling the H_2O excitation and dust continuum in Mrk231, G-A10 interpreted that collisional excitation from a cool extended region (610 pc, 41 K) is responsible for part of the low-lying line excitation, while IR pumping through far-IR photons by compact warm dense gas (120 pc, 95 K) excites high-lying lines and part of low-lying lines. The high abundance of H_2O can be explained as a consequence of shocks/cosmic rays and X-ray Dominated Regions (XDR) chemistry (Meijerink & Spaans 2005), and/or an undepleted chemistry (G-A10). Therefore, H_2O excitation is naturally linked to the local IRF, probing, e.g., the size and strength of the IR power source; tracing a different regime of gas than that of CO. Hence, it is important to have a systematic study of the H_2O lines in galaxies to better understand the gas excitation and physical processes within.

2. THE SAMPLE AND DATA REDUCTION

We used the *Herschel* Science Archive (HSA), containing both the SPIRE/Fourier Transform Spectrometer (FTS; Naylor et al. 2010) spectra at 450–1550 GHz, and the PACS (Poglitsch

---

et al. 2010) images at 70, 100, and 160 μm. Our sample consists of 45 sources with at least 1 rotational H_2O transition detected among 176 nearby galaxies available. The data are from 10 projects including *HerCULES* (PI: P. van der Werf) with an H_2O detection rate ∼80% and *GOALS* (PI: N. Lu., a full list can be found here: http://sfig.pmo.ac.cn/∼yangcht/h2oSample.txt). The typical SPIRE/FTS integration time is about several hours.

The data were reduced with HIPE v9 (Ott 2010). Basic steps of spectral data reduction contain background removal using off-axis detector subtraction and flux calibration with Neptune and Uranus, when available. Deglitch, flat field calibration through HIPE and brightness drift subtraction with Scanamorphos (Roussel 2012) have been used to reduce PACS images. All H_2O emission line detections are above the 3σ level. The instrumental sinc function has been adopted for the line fit using customized HIPE scripts, since the intrinsic line width is smaller than the instrumental resolution in most cases. However, although the flux could be underestimated by ∼20% for a few sources with very broad line widths such as Arp220, it is still insignificant when we consider the line fitting error (∼20%), the main source of the errors. Then we use the formula in Solomon et al. (1992) to convert line intensity (I_{H_2O}) to L_{H_2O}, taking the luminosity distance D_L in Sanders et al. (2003) ($H_0 = 75$ km s^{-1} Mpc^{-1}, $\Omega_M = 0.3$, and $\Omega_\Lambda = 0.7$; Mould et al. 2000).

After convolving *Spitzer*/MIPS 24 μm, PACS 70, 100, and 160 μm images to match with the SPIRE beams (Swinyard et al. 2010) following Aniano et al. (2011), we determine whether or not the source is extended based on its radial profile as compared with that of the corresponding Gaussian point-spread functions (PSFs). We use the total IR luminosities (8–1000 μm) from Sanders et al. (2003) as the L_{IR} for point sources. For extended galaxies, in-beam L_{IR} is calculated to ensure that L_{IR} and L_{H_2O} are spatially matched. First, we take the weighting coefficients of Galametz et al. (2013) to combine MIPS 24, PACS 70, 100, and 160 μm images into composite maps. Then the in-beam flux ratio between in-aperture and that of the entire source is derived with aperture photometries (FWHM of the Gaussian PSFs). It should be noted that the practically measured area by SPIRE/FTS is not limited in the FWHM beam, and we require an additional correction factor to account for this (D. Liu et al., in preparation). Applying this factor, we can then obtain the corrected in-beam fraction of the L_{IR} for extended sources. L_{IR} matched with the SPIRE beam can thus be obtained by applying this factor and the in-beam fraction to the global L_{IR} in Sanders et al. (2003). The full data set containing L_{IR} and L_{H_2O} will be described in D. Liu et al. (in preparation). Since we take the global flux density ratios of 25–60 μm (f_{25}/f_{60}) and 60–100 μm (f_{60}/f_{100}) as the IR colors (flux densities from Sanders et al. 2003) in a later analysis, we exclude the extended sources in these cases in order to keep the IR colors free from any contamination in spatial variations.

H_2O lines are also detected in the mapping mode data of M82, NGC 1068, and NGC 253. However, we have dropped the M82 mapping mode data because the very weak detection is only in the central detector and we already have a robust detection in the single pointing mode. For NGC 253, we add all the spectral data to obtain a global spectrum. For NGC 1068, we have at least one H_2O line detection in seven detectors. These sources are obviously extended and excluded in the IR color analysis.

3. RESULTS AND DISCUSSION

In our sample we find that H_2O is the strongest molecular emitter after high-J CO ($J = 8$–7 to $J = 13$–12) in the SPIRE band. In some cases (∼13%), e.g., ESO320-G030, the strength of $H_2O(3_{21}-3_{12})$ is even stronger. Besides the H_2O emission lines, $H_2O(1_{11}-0_{00})$ is detected in absorption in three sources, including Arp220 as reported by Rangwala et al. (2011). H_2O^+ absorption lines were also detected in a few sources (D. Liu et al. in preparation). In addition, emission lines of H_2O^+ and $H_2^{18}O$ are detected (Section 3.3). Those ionic molecules are the intermediate species for the main route of gas-phase H_2O formation.

3.1. Relation between H_2O and IR Luminosities

The correlation between L_{H_2O} for different transitions and L_{IR} was analyzed by two different methods: a Bayesian approach, LINMIX_ERR (Kelly 2007), and the nonlinear χ^2 fitting routine, MPFIT (Markwardt 2009). In Figure 1, we plot the luminosities of $H_2O(1_{11}-0_{00})$, $H_2O(2_{02}-1_{11})$, $H_2O(2_{11}-2_{02})$, $H_2O(2_{20}-2_{11})$, $H_2O(3_{12}-3_{03})$, $H_2O(3_{21}-3_{12})$, $H_2O(4_{22}-4_{13})$, and $H_2O(5_{23}-5_{14})$ (lines 1 to 8 hereafter) against the corresponding L_{IR}. In addition to our sample, we also include five high-z ULIRGs (Omont et al. 2013, see online Table 4) and HLSJ0918+5144 (Combes et al. 2012) in our fit for lines 2 and 3 (Figure 1). The QSO APM08279+5255 at $z = 3.9$ (van der Werf et al. 2011) is also added for comparison.

The two fitting methods yield similar results in log–log space over four orders of magnitude of the luminosity range. The fit can be described as

$$\log L_{H_2O} = \alpha \log L_{IR} + \beta. \tag{1}$$

The derived parameters are listed in Table 1. All values of α are close to 1, i.e., a linear relation, though the α given by the Bayesian approach are closer to linear. However, the α of lines 3 and 4 are a bit higher than that of the other lines. This is weakly significant when we consider the errors. The α of lines 2 and 3 are consistent with Omont et al. (2013). As the slopes are close to linear, we perform an additional linear fit by fixing $\alpha = 1$, and use χ^2 fitting to determine the constant ratios between L_{H_2O} and L_{IR}. These ratios vary from 3.3×10^{-6} for $H_2O(1_{11}-0_{00})$ to 1.1×10^{-5} for $H_2O(3_{21}-3_{12})$ (see the gray dashed lines and text in Figure 1 and Table 1). Because the detections of lines 1, 7, and 8 are not statistically significant, more data are needed to solidify the fits. In Figure 1, we find most of the $H_2O(2_{11}-2_{02})$ and $H_2O(3_{21}-3_{12})$ upper limits for the non-detections are consistent with the correlation. All the (U)LIRGs have a strong H_2O emission compatible with the correlation pointing out to a rather large H_2O abundance as known in shocked regions (e.g., G-A10; Harwit et al. 1998). Unlike the case in the Orion Bar, the proto-typical photodissociation region (PDR), where CO lines are a factor $\gtrsim 50$ stronger than the H_2O lines, the high H_2O/CO ratio of most sources in our sample makes it unlikely that those strong H_2O emission originate in classical PDRs (e.g., G-A10). The high CO/H_2O ratio in M82 (∼40; Weiß et al. 2010) indicates that it is dominated by classical PDRs, and thus has much weaker H_2O lines. As in Weiß et al. (2010), the H_2O lines in M82 are found to be very weak, nearly an order of magnitude below the correlation. It would be important to analyze the weak H_2O emission in other galaxies such as M82, but it is beyond the scope of this work. Therefore, we excluded M82 from our fit. Additionally, when we fit the correlations for L_{H_2O-2} and L_{H_2O-3} without high-z ULIRGs, we get slightly lower slopes. This means that high-z ULIRGs at the high L_{IR} end have slightly higher L_{H_2O}/L_{IR}.

The linear correlation could be the result of the very intense far-IR radiation via IR pumping. After the absorption of far-IR

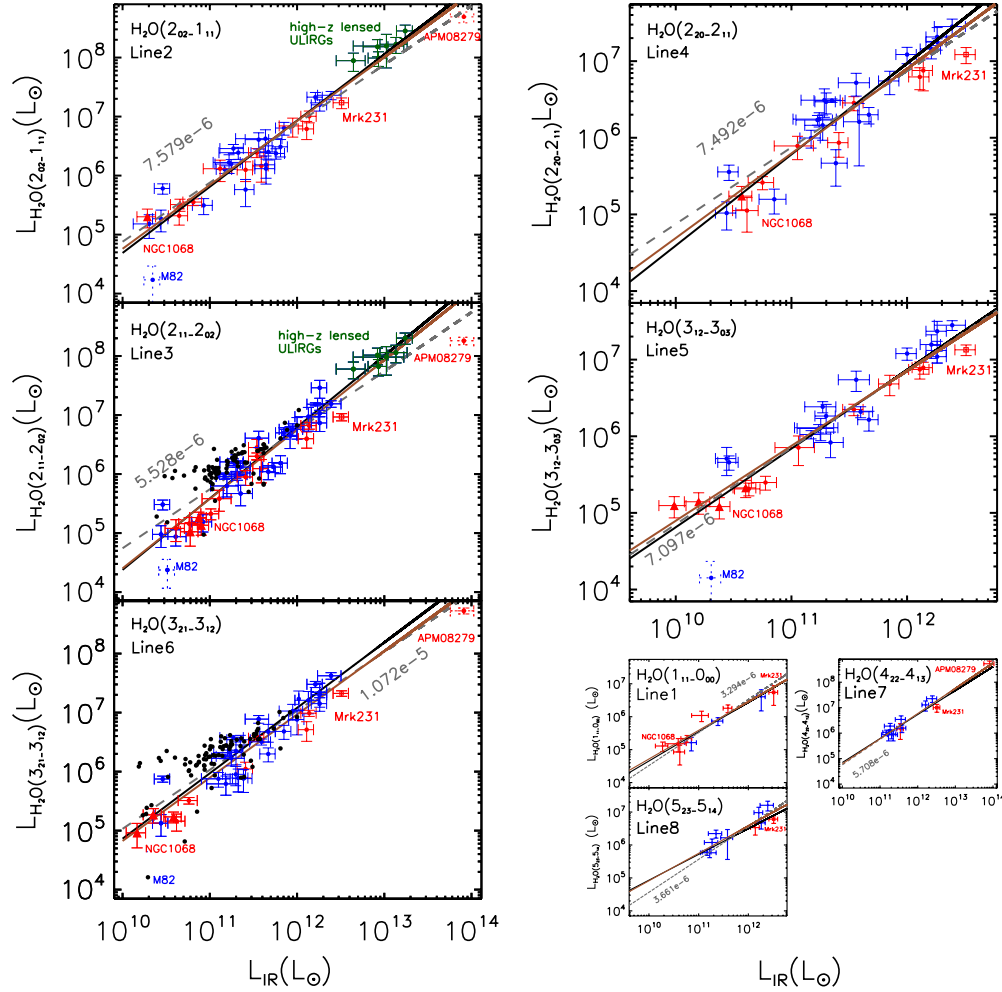**Figure 1.** Correlation between L_{H_2O} and the corresponding L_{IR} of our sample. The fitted lines by `MPFIT` and `LINMIX_ERR` are shown in black and brown lines, respectively, while the gray lines are the linear fitting with a fixed slope ($\alpha = 1$). The red, blue, green, and black dots represent strong-AGN, H II+mild-AGN-dominated galaxies, high-z ULIRGs, and the upper limits for non-detections, respectively. The solid triangles are the mapping mode data of NGC 1068. Mrk231 is marked in red squares. M82 and APM08279+5255, marked with dashed error bars, are excluded from the fitting.

(A color version of this figure is available in the online journal.)

Table 1
Fitted Parameters of the Correlations between H_2O Lines and L_{IR} (Equation (1))

H_2O Line	ν_{rest}(GHz)	α_{χ^2}	α_{Bayes}	β_{χ^2}	β_{Bayes}	$\langle L_{H_2O}/L_{IR} \rangle$
1, 1_{11}–0_{00} [a]	1113.343	0.89 ± 0.09	0.86 ± 0.17	-4.24 ± 1.06	-3.76 ± 1.94	3.29×10^{-6}
2, 2_{02}–1_{11}	987.927	1.12 ± 0.04	1.08 ± 0.05	-6.52 ± 0.47	-6.07 ± 0.59	7.58×10^{-6}
3, 2_{11}–2_{02}	752.033	1.21 ± 0.04	1.18 ± 0.06	-7.72 ± 0.49	-7.34 ± 0.67	5.53×10^{-6}
4, 2_{20}–2_{11}	1228.789	1.19 ± 0.06	1.10 ± 0.08	-7.30 ± 0.69	-6.33 ± 0.97	7.49×10^{-6}
5, 3_{12}–3_{03}	1097.365	1.03 ± 0.04	0.98 ± 0.06	-5.45 ± 0.51	-4.88 ± 0.65	7.10×10^{-6}
6, 3_{21}–3_{12}	1162.912	1.11 ± 0.05	1.07 ± 0.09	-6.22 ± 0.57	-5.88 ± 1.05	1.07×10^{-5}
7, 4_{22}–4_{13} [a]	1207.639	0.94 ± 0.12	0.84 ± 0.22	-2.91 ± 1.12	-3.43 ± 2.51	5.71×10^{-6}
8, 5_{23}–5_{12} [a]	1410.618	0.78 ± 0.10	0.99 ± 0.19	-4.56 ± 1.37	-4.93 ± 2.30	3.66×10^{-6}

Notes. [a] The resulting parameters of 1_{11}–0_{00}, 4_{22}–4_{13}, and 5_{23}–5_{12} contain large uncertainties due to the small sample size.
α_{χ^2} and β_{χ^2} are the slope and intercept from χ^2 fitting, while α_{Bayes} and β_{Bayes} are from the Bayesian method.

photons, the upper level H_2O molecules cascade toward the lines we observed in an approximately constant fraction. Thus, the H_2O luminosity should be linearly correlated with the IR emission. Though detailed excitation modeling is required, this linear correlation already shows the importance of IR pumping.

Using the NASA/IPAC Extragalactic Database (NED), we have separated our sample into two groups: optically identified, strong, active-galactic-nucleus-(AGN)-dominated (Seyfert

types 1 and 2) and star-forming-dominated galaxies possibly with mild AGNs (classes H II, composite and LINER of Kewley et al. 2006, hereafter "H II+mild-AGN"), as red and blue points in Figure 1, respectively. There is no obvious difference between these two groups and they both exhibit similar correlations. This implies that both strong-AGN and H II+mild-AGN sources behave similarly in H_2O emission, and a strong AGN may have little impact on the H_2O excitation. Although the

Table 2
Correlations between $(L_{H_2O}/L_{IR})/L_{IR}$, Different H_2O Line Ratios, and IR Colors, L_{IR}

Ratio	$R_{\log(f_{25}/f_{60})}$	$R_{\log(f_{60}/f_{100})}$	$R_{\log(L_{IR})}$	$\langle$strong$-$AGN$\rangle$	$\langle$H II + mild$-$AGN$\rangle$
2/IR, $2_{02}-1_{11}$/IR	-0.51	-0.25	-0.10	6.4×10^{-6}	9.2×10^{-6}
3/IR, $2_{11}-2_{02}$/IR	-0.51	0.17	-0.39	3.8×10^{-6}	5.8×10^{-6}
4/IR, $2_{20}-2_{11}$/IR	-0.55	-0.03	-0.21	5.0×10^{-6}	9.2×10^{-6}
5/IR, $3_{12}-3_{03}$/IR	-0.40	-0.02	-0.18	5.1×10^{-6}	9.4×10^{-6}
6/IR, $3_{21}-3_{12}$/IR	-0.67	-0.07	-0.17	6.7×10^{-6}	10.8×10^{-6}
2/3, $2_{02}-1_{11}/2_{11}-1_{02}$	0.16	-0.50	-0.38	1.50	1.52
2/4, $2_{02}-1_{11}/2_{20}-2_{11}$	0.16	-0.38	-0.47	1.09	1.09
2/5, $2_{02}-1_{11}/3_{12}-3_{03}$	-0.11	-0.28	0.25	1.14	0.88
2/6, $2_{02}-1_{11}/3_{21}-3_{12}$	0.56	-0.07	-0.20	0.87	0.72
3/4, $2_{11}-2_{02}/2_{20}-2_{11}$	0.10	0.35	0.08	0.61	0.63
3/5, $2_{11}-2_{02}/3_{12}-3_{03}$	-0.26	0.14	0.47	0.62	0.52
3/6, $2_{11}-2_{02}/3_{21}-3_{12}$	0.47	0.11	0.15	0.50	0.48
4/5, $2_{20}-2_{11}/3_{12}-3_{03}$	-0.15	-0.11	0.38	1.00	0.58
4/6, $2_{20}-2_{11}/3_{21}-3_{12}$	0.37	0.09	0.19	0.73	0.62
5/6, $3_{12}-3_{03}/3_{21}-3_{12}$	0.53	0.17	-0.21	0.69	0.65

Notes. $R_{\log(f_{25}/f_{60})}$, $R_{\log(f_{60}/f_{100})}$, and $R_{(L_{IR})}$ are the correlation coefficients between $\log[(L_{H_2O}/L_{IR})/L_{IR}]$, $\log[(L_{H_2O}/L_{IR})_a/(L_{H_2O}/L_{IR})_b]$, $\log(f_{25}/f_{60})$, $\log(f_{60}/f_{100})$, and $\log(L_{IR})$, respectively (see the text). $\langle$strong$-$AGN$\rangle$ and $\langle$H II + mild$-$AGN$\rangle$ are the error-weighted mean values of $(L_{H_2O}/L_{IR})/L_{IR}$ and $(L_{H_2O}/L_{IR})_a/(L_{H_2O}/L_{IR})_b$ for strong-AGN- and star-forming-dominated galaxies (see the text), respectively.
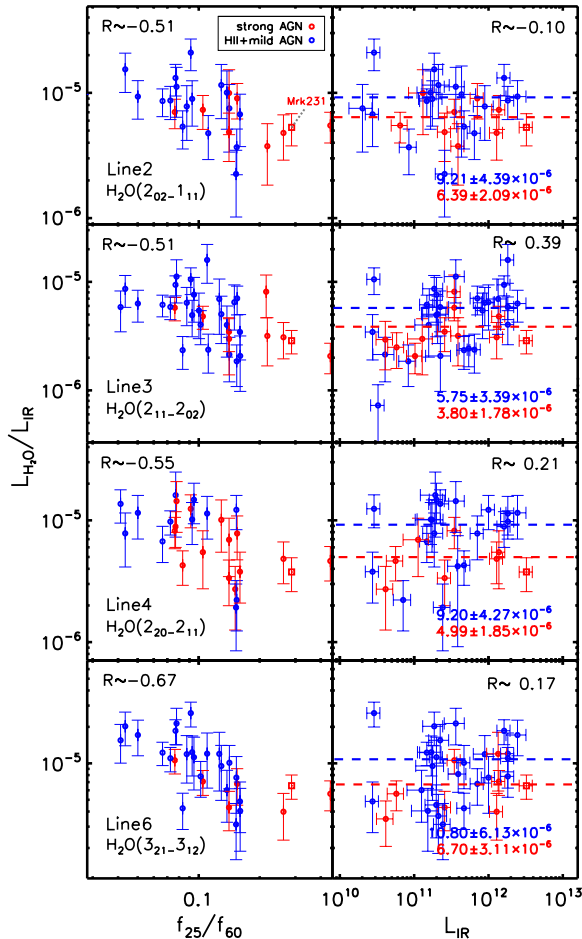

Figure 2. L_{H_2O}/L_{IR} vs. f_{25}/f_{60} and L_{IR}, respectively. From top to bottom, each row displays the values of lines 2, 3, 4, and 6 as examples. The averaged values of L_{H_2O}/L_{IR} of strong-AGN- and H II+mild-AGN-dominated sources are shown in red and blue text and dashed lines in the second column. R in each panel is the correlation coefficient. Mrk231 is shown in red squares. The blue and red colors are the same as in Figure 1.

(A color version of this figure is available in the online journal.)

number of statistics is small, the detection rate of H II+mild-AGN ($\sim 3.2\%$) is lower than strong AGN ($\sim 12.4\%$) for $H_2O(1_{11}-0_{00})$. The remaining H_2O lines have comparable detection rates of both kinds, and lines 2 and 3 have the highest detection rate of about 30%. The absence of an apparent significant AGN contribution indicates that an AGN may not be the main power source of the H_2O excitation. The origin of such abundant H_2O reservoir might thus favor an undepleted chemistry or shocks/cosmic rays rather than XDR chemistry (G-A10).

We then analyzed the correlation between L_{H_2O}/L_{IR} and the IR colors, along with the L_{IR} (Figure 2 and Table 2). We dismiss lines 1, 7, and 8 here for their insignificant statistics because hardly any correlation has been found between L_{H_2O}/L_{IR} and f_{60}/f_{100} (Table 2). We find, however, that L_{H_2O}/L_{IR} ratios decrease with the increasing f_{25}/f_{60}, with significant correlation coefficients ($R \sim -0.5$). A similar correlation has also been found in lines 7 and 8, though with low statistics. This correlation may be explained by a smaller contribution to the submillimeter H_2O line excitation from very warm dust radiation (dust temperature $T_d \sim 110$ K) than from warm dust ($T_d \sim 50$ K). We also find that line 6 has the largest $R \sim -0.7$, possibly indicating that this transition is more sensitive to T_d than others. There is no significant correlation between L_{H_2O}/L_{IR} and L_{IR} except for line 3 ($R \sim 0.4$), as shown in the second column of Figure 2 and in Table 2. This seems to be consistent with the slightly super-linear relation found for L_{H_2O-3} with L_{IR} (Figure 1). The non-variation of L_{H_2O}/L_{IR} with L_{IR} for most lines confirms the validity of the near-linear relations in Figure 1.

Again, here we separate the sources into strong-AGN and H II+mild-AGN as in Figure 1. It appears that strong AGNs, on average, have higher f_{25}/f_{60} compared with the others. This is a well-known property of AGN sources that have more very warm dust than starburst sources (e.g., Younger et al. 2009). However, both strong-AGN and H II+mild-AGN species show a similar trend for the variation of L_{H_2O}/L_{IR} with f_{25}/f_{60}. Their different IR colors might cause the average value of L_{H_2O}/L_{IR} in strong AGNs to be slightly lower, by about 40%, than in H II+mild-AGN sources for all lines (Figure 2 and Table 2), but the difference is hardly significant.
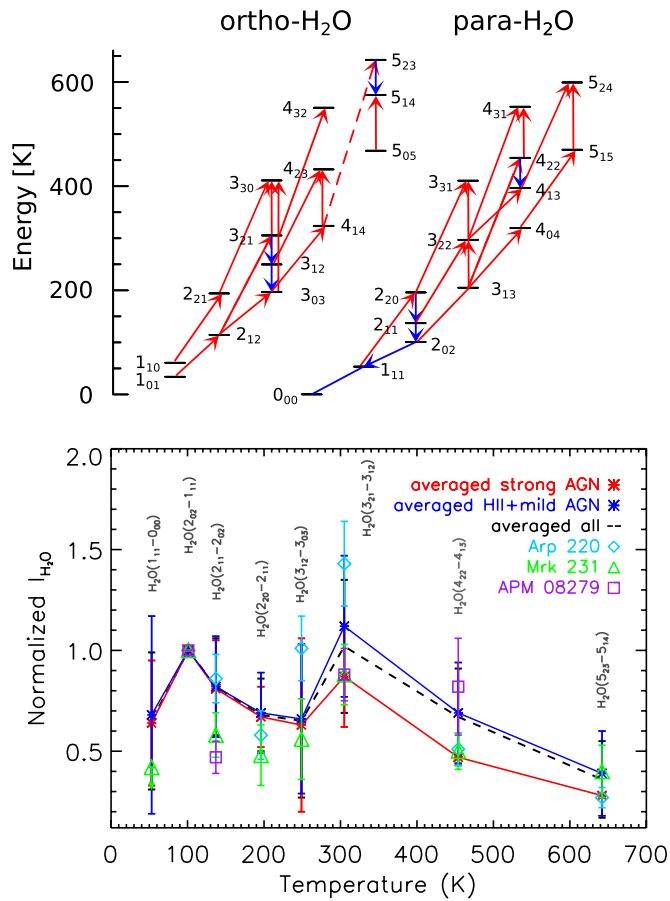
Figure 3. Upper panel shows the H_2O energy level diagram. Among the red lines that indicate the main possible IR pumping paths, the solid lines show the observed absorption lines in Mrk231, Arp220 and NGC 4418 (G-A10; González-Alfonso et al. 2012). The blue lines are the transitions we detected. The lower panel shows the $I_{H_2O(2_{02}-1_{11})}$ normalized H_2O intensities (in Jy km s^{-1}). The black dashed line represents the average values of the whole sample, while red and blue points and lines are those of the strong-AGN- and H II+mild-AGN-dominated galaxies, respectively. The green and light blue symbols represent Mrk231 (G-A10) and Arp220 (Rangwala et al. 2011), respectively. The purple squares represent the lensed QSO APM08279+5255 (van der Werf et al. 2011).

(A color version of this figure is available in the online journal.)

3.2. H_2O Line Ratios and the Average Spectral Line Energy Distribution (SLED)

Line ratios between different transitions could help us understand the excitation of H_2O and the physical condition of the warm dense gas. Thus, we compare the H_2O line ratios with IR colors and luminosities. As discussed in Section 2, different transitions have various beam sizes. In order to compare different H_2O transitions, we have to remove this beam size dependence. We simply do this by dividing L_{H_2O} by L_{IR} since they are linearly correlated. Thus, $(L_{H_2O}/L_{IR})_a/(L_{H_2O}/L_{IR})_b$ (a/b[10] hereafter) could represent the true luminosity ratio between two H_2O lines, a and b. Table 2 lists the results. In Figure 2, $(L_{H_2O}/L_{IR})_6$ has the steepest dependence on f_{25}/f_{60} compared with other lines. Thus, the ratio between L_{H_2O}/L_{IR} of any other line and $(L_{H_2O}/L_{IR})_6$ should have a correlation with f_{25}/f_{60}. Indeed, as we can see in the table, where the R for line ratios 2/6, 3/6, and 5/6 versus f_{25}/f_{60} is $\gtrsim 0.5$. Also the line ratio 2/3 decreases

---

^{10} a, b represent different H_2O lines at different frequencies with different FTS beam sizes.

with increasing f_{60}/f_{100} ($R \sim -0.5$). Although there are some R close to ± 0.5 for the correlation between I_{H_2O}/L_{IR} and L_{IR}, these trends may not be real for they are within the error. The low line ratio 2/6 in Table 2 might indicate that IR pumping is important since collisional excitation alone cannot explain the high intensities of the high-lying lines compared with low-lying lines (e.g., G-A10).

In order to have a general view of the H_2O excitation, we calculate the error-weighted average line intensity ratios with respect to $H_2O(2_{02}-1_{11})$. In Figure 3, the upper panel shows the H_2O energy level diagram. The lower panel of Figure 3 shows an average H_2O SLED together with SLEDs taken from previous case studies (G-A10; van der Werf et al. 2011; Rangwala et al. 2011). The individual studies agree well with our averaged SLED. All SLEDs show two peaks at $H_2O(2_{02}-1_{11})$ and $H_2O(3_{21}-3_{12})$, and the latter is slightly stronger. The explanation for the strong high-lying peak could be that the IR spectral energy distribution (SED) peaks are close to 75 μm which could result in higher IR pumping efficiency considering the possibility of IR pumping at 75 μm (Figure 3, upper panel) which is the main power source of $H_2O(3_{21}-3_{12})$ and $H_2O(3_{12}-3_{03})$ (G-A10). However, we should be cautious in this interpretation because the H_2O line intensities depend not only on the excitation conditions, but also on the intrinsic line strengths of the H_2O molecule. Detailed excitation modeling is therefore needed. The high-lying lines to $H_2O(2_{02}-1_{11})$ ratios in H II+mild-AGNs appear a bit stronger than strong AGNs (Figure 3 and Table 2). In Section 3.1, we find that the high-lying lines have steeper anti-correlation on f_{25}/f_{60}, thus strong AGNs, with higher f_{25}/f_{60}, are expected to show lower high-lying lines to $H_2O(2_{02}-1_{11})$ ratios.

3.3. Emission Lines of H_2O-related Ionic and Isotope Molecules

Besides H_2O, the related ionic and ^{18}O isotope molecular emission lines are also found. H_2O^+ forms via ionization of H and H_2, after the combination of H_2, it forms H_3O^+, and the recombination with electrons leads to OH and H_2O (Hollenbach et al. 2012). Among 45 H_2O-detected sources, 5 have $H_2O^+(1_{11}-0_{00},J_{3/2,1/2})$ (1115.204 GHz), another 5 have $H_2O^+(1_{11}-0_{00},J_{1/2,1/2})$ (1139.561 GHz), 12 have $H_2O^+(2_{02}-1_{11},J_{3/2,3/2})$ (746.194 GHz), 7 sources have H_2O^+ $(2_{02}-1_{11},J_{5/2,3/2})$ (742.033 GHz), and 3 have $H_2^{18}O(3_{21}-3_{12})$ (1136.704 GHz) detected. Both strong-AGN- and H II+mild-AGN-dominated galaxies are among these detections. We find their luminosities to be tightly correlated with those of the related H_2O transitions. Taking $H_2O^+(2_{02}-1_{11},J_{3/2,3/2})$, which has the largest number of detections as an example, the luminosities of $H_2O^+(2_{02}-1_{11},J_{3/2,3/2})$ and $H_2O(2_{02}-1_{11})$ perfectly fit a linear correlation. $H_2O^+(2_{02}-1_{11})$ lines are about 4.5 times weaker than $H_2O(2_{02}-1_{11})$ and 2.5 times weaker than $H_2O(2_{11}-2_{02})$, while the strength of $H_2O^+(1_{11}-0_{00})$ is almost the same as that of $H_2O(1_{11}-0_{00})$. These preliminary results are important for further observations of those ionic diagnostic lines in high-z galaxies, although the number of the sources ($\lesssim 10$) is not sufficient to draw any concrete conclusion at this stage.

4. CONCLUSIONS

H_2O is found to be the second strongest molecular emitter in our sample of 45 nearby IR galaxies after high-J CO lines within the SPIRE/FTS band. Near-linear correlations have been found between various H_2O rotational transitions and corresponding

L_{IR}, whereas $H_2O(2_{11}-2_{02})$ and $H_2O(2_{20}-2_{11})$ may have slightly steeper slopes. The ratios of L_{H_2O}/L_{IR} vary with f_{25}/f_{60}, while nearly no trend with f_{60}/f_{100} and L_{IR} has been found, indicating that very warm dust contributes little to the H_2O excitation. The near constant L_{H_2O}/L_{IR} ratios reveal an intrinsic linear correlation, regardless of whether or not a strong AGN is present. We find no significant difference in the correlation between strong-AGN- and star-forming-dominated galaxies, although strong AGNs might have slightly smaller average ratios L_{H_2O}/L_{IR}. In less than one-third of both kinds of galaxies, related ionic H_2O^+ emission lines have been detected, while their strength tightly correlates with that of the corresponding H_2O lines. $H_2^{18}O$ isotope line emission is also detected in three sources. It seems that the IR pumping at 75 μm, the IR SED peak, is most important in excitation of high-lying H_2O lines in these IR galaxies. Nevertheless, detailed modeling is needed, e.g., Large Velocity Gradient or XDR models, in order to derive some physical parameters of the H_2O excitation and to provide a quantitative diagnostic tool of the IR radiation field and warm dense gas in galaxies other than CO lines.

REFERENCES

Aniano, G., Draine, B. T., Gordon, K. D., & Sandstorm, K. 2011, PASP, 123, 1218
Combes, F., Rex, M., Rawle, T. D., et al. 2012, A&A, 538, L4
Galametz, M., Kennicutt, R. C., Calzetti, D., et al. 2013, MNRAS, 431, 1956
Goicoechea, J. R., Martín-Pintado, J., & Cernicharo, J. 2005, ApJ, 619, 291
González-Alfonso, E., Fischer, J., Bruderer, S., et al. 2013, A&A, 550, A25
González-Alfonso, E., Fischer, J., Graciá-Carpio, J., et al. 2012, A&A, 541, A4
González-Alfonso, E., Fischer, J., Isaak, K., et al. 2010, A&A, 518, L43
González-Alfonso, E., Smith, H. A., Ashby, M. L. N., et al. 2008, ApJ, 675, 303
González-Alfonso, E., Smith, H. A., Fischer, J., & Cernicharo, J. 2004, ApJ, 613, 247
Griffin, M. J., Abergel, A., Abreu, A., et al. 2010, A&A, 518, L3
Harwit, M., Neufeld, D. A., Melnick, G. J., & Kaufman, M. J. 1998, ApJL, 497, L105
Hollenbach, D., Kaufman, M. J., Neufeld, D., et al. 2012, ApJ, 754, 105
Kamenetzky, J., Glenn, J., Rangwala, N., et al. 2012, ApJ, 753, 70
Kelly, B. C. 2007, ApJ, 665, 1489
Kessler, M. F., Steinz, J. A., Anderegg, M. E., et al. 1996, A&A, 315, L27
Kewley, L. J., Groves, B., Kauffmann, G., & Heckman, T. 2006, MNRAS, 372, 961
Markwardt, C. B. 2009, in ASP Conf. Ser. 411, Astronomical Data Analysis Software and Systems XVIII, ed. D. A. Bohlender, D. Durand, & P. Dowler (San Francisco, CA: ASP), 251
Meijerink, R., Kristensen, L. E., Weiß, A., et al. 2013, ApJL, 762, L16
Meijerink, R., & Spaans, M. 2005, A&A, 436, 397
Melnick, G. J., & Bergin, E. A. 2005, AdSpR, 36, 1027
Mould, J. R., Huchra, J. P., Freedman, W. L., et al. 2000, ApJ, 529, 786
Naylor, D. A., Baluteau, J.-P., Barlow, M. J., et al. 2010, Proc. SPIE, 7731, 773116
Omont, A., Neri, R., Cox, P., et al. 2011, A&A, 530, L3
Omont, A., Yang, C., Cox, P., et al. 2013, A&A, 551, A115
Ott, S. 2010, in ASP Conf. Ser. 434, Astronomical Data Analysis Software and Systems XIX, ed. Y. Mizumoto, K.-I. Morita, & M. Ohishi (San Francisco, CA: ASP), 139
Pilbratt, G. L., Riedinger, J. R., Passvogel, T., et al. 2010, A&A, 518, L1
Poglitsch, A., Waelkens, C., Geis, N., et al. 2010, A&A, 518, L2
Rangwala, N., Maloney, P. R., Glenn, J., et al. 2011, ApJ, 743, 94
Riechers, D. A., Bradford, C. M., Clements, D. L., et al. 2013, Natur, 496, 329
Roussel, H. 2012, arXiv:1205.2576
Sanders, D. B., Mazzarella, J. M., Kim, D.-C., Surace, J. A., & Soifer, B. T. 2003, AJ, 126, 1067
Solomon, P. M., Downes, D., & Radford, S. 1992, ApJL, 398, L29
Spinoglio, L., Pereira-Santaella, M., Busquet, G., et al. 2012, ApJ, 758, 108
Swinyard, B. M., Ade, P., Baluteau, J.-P., et al. 1010, A&A, 518, L4
van der Werf, P. P., Berciano Alba, A., Spaans, M., et al. 2011, ApJL, 741, L38
van der Werf, P. P., Isaak, K. G., Meijerink, R., et al. 2010, A&A, 518, L42
van Dishoeck, E. F., Kristensen, L. E., Benz, A. O., et al. 2011, PASP, 123, 138
Weiß, A., Requena-Torres, M. A., & Güsten, R. 2010, A&A, 521, L1
Younger, J. D., Hayward, C. C., Narayanan, D., et al. 2009, MNRAS, 396, L66